Sustainable Marine Structures
https://ojs.nassg.org/index.php/sms

ARTICLE

Comparison of Potential Theory and Morison Equation for Deformable Horizontal Cylinders

Chungkuk Jin*

Department of Ocean Engineering, Texas A&M University, Texas, the United States

ARTICLE INFO

Article history
Received: 18 February 2022
Accepted: 10 March 2022
Published Online: 30 March 2022

Keywords:
Wave force
Discrete-module-beam method
Potential theory
Morison equation
Horizontal cylinder

ABSTRACT

This study investigates the hydro-elastic behaviors of fully submerged horizontal cylinders in different regular waves. Two methods were proposed and compared in this study. The first method was based on potential theory in frequency domain and the discrete-module-beam (DMB) method, which discretizes a floating elastic structure into a sufficient number of rigid bodies while simultaneously representing the elastic behavior from beam elements with Euler-Bernoulli beam and Saint-Venant torsion. Moreover, the Morison method in time domain was employed; this method estimates wave forces from the semi-empirical Morison equation, and the elastic behavior is embodied by massless axial, bending, and torsional springs. Various parametric studies on cylinder diameter, submergence depth, and wave direction were conducted. Wave forces, dry/wet mode shapes/natural frequencies, and dynamic motions are presented and analyzed.

1. Introduction

Underwater cylindrical structures have been suggested for various reasons. Many of them lie on the seabed, and typical examples include submarine pipelines that transport water, oil, and natural gas, submarine cables for electricity transmission, and immersed tunnels for public transportation. Even if these structures have accumulated engineering practices, several critical limitations still exist. These structures are susceptible to seismic activities [1,2]; the seabed should be even for installation; scours, the removal of sediment around the pipeline, can occur and are critical for vibration and fatigue damage associated with seabed movement [3]. Also, the deepwater application is very challenging for submarine pipelines and cables due to not only high hydrostatic pressure and temperature difference but also high costs associated with a longer length and additional intervention work for the seabed [4].

Submerged floating structures have been proposed as novel alternatives to the above structures, and representative examples are submerged floating pipelines and submerged floating tunnels. These structures float at a submergence depth and keep their location with mooring

*Corresponding Author:
Chungkuk Jin,
Department of Ocean Engineering, Texas A&M University, Texas, the United States;
Email: jinch999@tamu.edu

DOI: http://dx.doi.org/10.36956/sms.v4i2.492
Copyright © 2022 by the author(s). Published by Nan Yang Academy of Sciences Pte Ltd. This is an open access article under the Creative Commons Attribution-NonCommercial 4.0 International (CC BY-NC 4.0) License. (https://creativecommons.org/licenses/by-nc/4.0/).

systems if needed. They have several advantages: (1) they can be safe from wave and seismic actions by properly selecting design parameters, (2) the deepwater application is much more straightforward without considerable hydrostatic pressure and temperature difference, as in the deepwater location, and (3) structural health monitoring is much easier [4-9].

Their considerable dynamic and structural behavior and the resulting large mooring tension are still considered severe under various environmental conditions such as waves, currents, earthquakes, and tsunamis. Many studies adopted the Morison equation [10] for force estimation of the horizontal cylinder [11-13] due to low computational cost. However, the Morison equation has limitations in that wavelength should be more than five times the characteristic length ($D/L \le 0.2$ where D is cylinder diameter and L is wavelength), and the radiation effect is neglected. In addition, when the structure is close to free surface, the free-surface effect can be substantial, which results in a considerable variation of the scattering wave force compared with the deeply submerged structure cases [14]. The resulting mooring tension can also be different to a great extent. In this regard, validation work of the Morison equation for fully submerged floating structures is essential with respect to different diameters, submergence depths, and wave directions.

Several papers discussed the validity of the Morison equation by comparing it with theory-based approaches. Typically, the inertia coefficient C_M is fixed at 2 according to the slender body assumption and can vary for the non-slender body. For example, Chakrabarti and Tam [15] estimated the effective inertia coefficient for the Morison equation for bottom-mounted surface-piecing vertical cylinder and proved that the effective inertia coefficient significantly decreases as D/L increases. Chung [16] stated that when an object is close to free surface, the inertia coefficient can be a function of frequency, and radiation damping can be empirically added. In other words, its validity may be weakened when the free-surface effect exists to a great degree. Chang et al. [17] showed that the Morison equation reasonably estimates wave force up to second order for the hinged vertical cylinder at small wave steepness. However, they also mentioned that the Morison equation underestimates the peak wave force and overestimates trough wave forces at high wave steepness. Varying inertia coefficients along the submergence depth are proposed as in Ref. [18]. Regarding horizontal cylinders, Li et al. [19] conducted experimental studies for in-line responses for a submerged horizontal cylinder and showed that the inertia coefficient is not changing significantly with respect to the Keulegan-Carpenter number as opposed to vertical cylinders. Chen et al. [20] compared the Morison equation with CFD simulation and showed that the Morison equation underestimates the wave force on a partially submerged horizontal cylinder by up to 50% relative errors.

This study compared the potential theory with the Morison equation for fully-submerged horizontal cylinders. Both ends were fixed with the fixed-fixed boundary condition in which there are no displacements and angles at both ends. The multibody-based hydro-elasticity method with the potential theory in frequency domain—referred to as the discrete-module-beam (DMB) method—was compared with the lumped mass method with Morison equation—referred to as the Morison method. The Froude-Krylov, scattering wave, and radiation damping forces in the DMB method were compared with the inertia force of the Morison equation in the Morison method. Dry/wet natural frequencies/mode shapes and horizontal/vertical motions/forces were systematically presented and analyzed.

2. Theory and Formulation

Two different approaches were selected to evaluate dynamic behaviors and wave forces for a fully submerged horizontal cylinder. The first method was the DMB method, in which wave forces are estimated by 3-dimensional (3D) potential theory in frequency domain and Euler-Bernoulli beam and Saint-Venant torsion are employed for representing elastic behaviors. The second method is the Morison method, in which the Morison equation estimates wave forces with representative added mass and inertia coefficients in time domain while beam elements are modeled by the lumped mass method with massless axial, bending, and torsional springs. The theory and formulation of the two methods are explained in this section. Detailed formulations regarding the two methods and their validations can be found in Refs [12,21,22].

2.1 Discrete-Module-Beam Method in Frequency Domain

The DMB method is based on 3D potential theory for the multibody in frequency domain; a large deformable structure consists of M rigid bodies and $M-1$ connecting beams [23,24], as shown in Figure 1. The DMB method uses the right-handed Cartesian coordinate system.

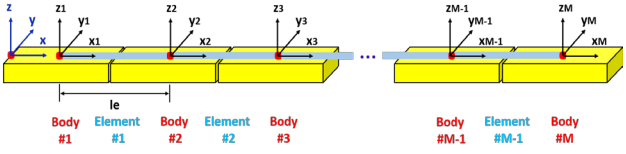

Figure 1. DMB method [25].

Laplace equation is governing equation for the potential theory when fluid is incompressible, irrotational, and inviscid as:

$$\begin{aligned}&\nabla^2\Phi=0\\&\Phi=\varphi e^{-i\omega t}\end{aligned}\tag{1}$$

where Φ is the total time-dependent velocity potential, which can be decomposed into the total time-independent velocity potential φ and the time-dependent term $e^{-i\omega t}$ based on the assumption of harmonic excitation with wave angular frequency ω and time t. φ can further be decomposed into diffraction and radiation components with the incident, scattered, and radiation potentials φ_I, φ_S, and $\varphi_R^{(m)}$ as:

$$\begin{aligned}&\varphi=\varphi_I+\varphi_S+\sum_{m=1}^{M}\varphi_R^{(m)}\\&\varphi_R^{(m)}=-i\omega\sum_{j=1}^{6}\xi_j^{(m)}\varphi_{jR}^{(m)}\end{aligned}\tag{2}$$

where m represents the mth rigid body and $\xi_j^{(m)}$ is six degrees of freedom (6DOF) displacements of the mth rigid body, i.e., surge, sway, heave, roll, pitch, and yaw motions. First-order φ_I can be written as:

$$\varphi_I=\frac{igA_w}{\omega}\frac{\cosh k\left(z+H\right)}{\cosh kH}e^{ik(x\cos\theta+y\sin\theta)}\tag{3}$$

where A_w is the amplitude of an incident wave, k is the wavenumber, H is water depth, θ is the wave direction, and g is the gravity acceleration. Moreover, φ_S and $\varphi_R^{(m)}$ can be obtained by considering the following boundary conditions on the free surface S_F, bottom S_B, body $S_k\left(k=1,2,\ldots,M\right)$, and far-field S_∞ as:

$$\begin{aligned}&\left(-\omega^2+g\frac{\partial}{\partial z}\right)\varphi^{\times}=0 && \text{on } S_F\left(z=0\right)\\&\frac{\partial\varphi^{\times}}{\partial z}=0 && \text{on } S_B\left(z=-H\right)\\&\frac{\partial\varphi_S}{\partial n}=-\frac{\partial\phi_I}{\partial n} && \text{on } S_k\\&\frac{\partial\varphi_{jR}^{(m)}}{\partial n^{(k)}}=\begin{cases}n_j^{(m)}, & k=m\\0, & k\neq m\end{cases} && \text{on } S_k\\&\lim_{r\to\infty}\sqrt{r}\left(\frac{\partial}{\partial r}-ik\right)\varphi^{\times}=0 && \text{on } S_\infty\end{aligned}\tag{4}$$

where r is the radial distance from the origin. $\varphi^{\times}$ can be φ_S or $\varphi_{jR}^{(m)}$. $n_j^{(m)}$ is the inward unit normal vector for the j th DOF on the m th body surface with respect to the body-fixed coordinate system. φ_S and $\varphi_{jR}^{(m)}$ are obtained by the 3D boundary element method. Each body's coordinate center is its center of gravity.

The wave excitation force that is the sum of the Froude-Krylov and scattered wave forces for the j th DOF on the m th rigid body in the body-fixed coordinate system is given in Equation (5):

$$F_{jW}^{(m)}=i\rho\omega\iint_{S_m}\left(\varphi_I+\varphi_S\right)n_j^{(m)}dS\tag{5}$$

The radiation force for the j th DOF on the m th rigid body induced by the k th DOF of the n th rigid body in the body-fixed coordinate system is given in Equation (6):

$$F_{jkR}^{(mn)}=\omega^2A_{jk}^{(mn)}\xi_k^{(n)}+i\omega B_{jk}^{(mn)}\xi_k^{(n)}=\rho\omega^2\xi_k^{(n)}\iint_{S_m}\varphi_{kR}^{(n)}\frac{\partial\varphi_{jR}^{(m)}}{\partial n^{(m)}}dS\tag{6}$$

where $A_{jk}^{(mn)}$ and $B_{jk}^{(mn)}$ denote the added mass and radiation damping coefficients of the j th DOF of the m th rigid body induced by the k th DOF of the n th rigid body. In addition, the hydrostatic restoring force of the m th rigid body for the j th DOF is given in Equation (7):

$$F_{jH}^{(m)}=-\rho g\iint_{S_m}\left(\xi_3^{(m)}+\xi_4^{(m)}y_m-\xi_5^{(m)}x_m\right)n_j^{(m)}dS\tag{7}$$

After the hydrodynamic forces and coefficients have been introduced, the equation of motion for M rigid bodies can be written with the mass, added mass, radiation damping, hydrostatic restoring coefficient matrices, $\mathbf{M}$, $\mathbf{A}$, $\mathbf{B}$, and $\mathbf{K}$, and wave-excitation-force vector $\mathbf{F}_W$ as:

$$\left(\mathbf{M}+\mathbf{A}\left(\omega\right)\right)\ddot{\boldsymbol{\xi}}+\left(\mathbf{B}\left(\omega\right)+\mathbf{B_R}\right)\dot{\boldsymbol{\xi}}+\left(\mathbf{K}+\mathbf{K}_E\right)\boldsymbol{\xi}=\mathbf{F}_W\left(\omega\right)\tag{8}$$

where upper dot means time derivative and $\mathbf{B_R}$ is the structural damping matrix. In Equation (8), the external stiffness matrix $\mathbf{K}_E$ is introduced to consider the elastic behavior of a deformable floating structure. $\mathbf{K}_E$ is constructed with Euler-Bernoulli beam and Saint-Venant's torsion theory for $M-1$ beam elements. The 12 by 12 sub-stiffness matrix $\mathbf{K}_e$ for the e th beam element in the local coordinate system is given in Equation (9):

$$\mathbf{K}_e=\begin{bmatrix}
\frac{EA_c}{l_e} & & & & & & & & & & & \text{symm.}\\
0 & \frac{12EI_z}{l_e^3} & & & & & & & & & & \\
0 & 0 & \frac{12EI_y}{l_e^3} & & & & & & & & & \\
0 & 0 & 0 & \frac{GI_x}{l_e} & & & & & & & & \\
0 & 0 & -\frac{6EI_y}{l_e^2} & 0 & \frac{4EI_y}{l_e} & & & & & & & \\
0 & \frac{6EI_z}{l_e^2} & 0 & 0 & 0 & \frac{4EI_z}{l_e} & & & & & & \\
-\frac{EA_c}{l_e} & 0 & 0 & 0 & 0 & 0 & \frac{EA_c}{l_e} & & & & & \\
0 & -\frac{12EI_z}{l_e^3} & 0 & 0 & 0 & -\frac{6EI_z}{l_e^2} & 0 & \frac{12EI_z}{l_e^3} & & & & \\
0 & 0 & -\frac{12EI_y}{l_e^3} & 0 & \frac{6EI_y}{l_e^2} & 0 & 0 & 0 & \frac{12EI_y}{l_e^3} & & & \\
0 & 0 & 0 & -\frac{GI_x}{l_e} & 0 & 0 & 0 & 0 & 0 & \frac{GI_x}{l_e} & & \\
0 & 0 & -\frac{6EI_y}{l_e^2} & 0 & \frac{2EI_y}{l_e} & 0 & 0 & 0 & \frac{6EI_y}{l_e^2} & 0 & \frac{4EI_y}{l_e} & \\
0 & \frac{6EI_z}{l_e^2} & 0 & 0 & 0 & \frac{2EI_z}{l_e} & 0 & -\frac{6EI_z}{l_e^2} & 0 & 0 & 0 & \frac{4EI_z}{l_e}
\end{bmatrix}\tag{9}$$

where E and G are Young's and shear moduli, A_c is the cross-sectional area, l_e is the element length, and I_x, I_y, and I_z are the torsional, vertical, and lateral second moments of area about x, y, and z axes, respectively. $\mathbf{K}_E$ can be expressed for $M-1$ beam elements with the 6 by 6 sub-stiffness matrices of $\mathbf{K}_e$ as:

$$\mathbf{K}_E = \begin{bmatrix} \mathbf{K}_1^{(11)} & \mathbf{K}_1^{(12)} & 0 & \cdots & 0 \\ \mathbf{K}_1^{(21)} & \mathbf{K}_1^{(22)} + \mathbf{K}_2^{(11)} & \mathbf{K}_2^{(12)} & \cdots & 0 \\ 0 & \mathbf{K}_2^{(21)} & \mathbf{K}_2^{(22)} + \mathbf{K}_3^{(11)} & \cdots & 0 \\ \vdots & \vdots & \vdots & \ddots & \vdots \\ 0 & 0 & 0 & \cdots & \mathbf{K}_{M-1}^{(22)} \end{bmatrix} \quad (10)$$

$$\mathbf{K}_e = \begin{bmatrix} \mathbf{K}_e^{(ii)} & \mathbf{K}_e^{(ij)} \\ \mathbf{K}_e^{(ji)} & \mathbf{K}_e^{(jj)} \end{bmatrix}$$

2.2 Morison Method in Time Domain

The Morison method was also modeled in time domain [26]. In this method, a deformable floating structure consists of finite elements with nodes and segments. Key physical properties are included in the nodes while segments present structure's deformability with massless axial, bending, and torsional springs. The Morison equation evaluates the hydrodynamic forces for a moving body at its instantaneous node position. The computational time of this method is lower than the frequency-domain DMB method since this method is dependent on the Morison equation for wave-force estimation. It is worth utilizing this method if accurate global performance estimation is possible with a cheaper computational cost. The equation of motion for a deformable floating structure in time domain can be expressed as:

$$\mathbf{M}\ddot{\mathbf{X}} + \mathbf{B}_R\dot{\mathbf{X}} + \mathbf{K}_S\mathbf{X} = \mathbf{F}_M + \mathbf{w}$$
$$\mathbf{F}_M = -C_A\Delta\ddot{\mathbf{X}}^n + C_M\Delta\dot{\boldsymbol{\eta}}^n + \frac{1}{2}C_D\rho A\left|\boldsymbol{\eta}^n - \dot{\mathbf{X}}^n\right|\left(\boldsymbol{\eta}^n - \dot{\mathbf{X}}^n\right) \quad (11)$$

where $\mathbf{K}_S$ are the structural stiffness matrix, $\mathbf{F}_M$ is the hydrodynamic force vector based on the Morison equation, $\mathbf{w}$ is the wet-weight vector (i.e., buoyancy minus dry weight), C_A, C_M, and C_D are the added mass, inertia, and drag coefficients, Δ and A are the displaced mass and drag area, ρ is the seawater density, η and $\dot{\eta}$ are the velocity and acceleration vectors of fluid particles, and n denotes the normal direction. Structural deformability is represented by K_S with axial, bending, and torsional springs. The drag term of the Morison equation, i.e., 3rd term in Equation (11), was neglected since the Keulegan-Carpenter number of the presented problem is low (inertia dominant).

3. Case Description

Figure 2 shows the configuration of a concrete hollow cylinder. Its density and Young's modulus were 2300 kg/m^3 and 30 GPa. The length of the concrete cylinder was fixed at 500 m, whereas various diameters of 10 m–20 m, submergence depths of 20 m–60 m, and wave directions of 30°–90° were selected as design parameters. In this study, the cylinder's buoyancy-weight ratio was set at 1.0, which means its buoyancy is the same as its dry weight. Then, the inner diameter and axial, bending, and torsional stiffness were reversely estimated based on the given buoyancy-weight ratio. The fixed-fixed boundary condition at both ends was designed; in other words, displacements and angles at both ends do not change. Water depth was fixed at 100 m.

4. Results and Discussions

4.1 Wave Force

The wave excitation force $\mathbf{F}_W$ in potential theory is often correlated with the inertia force term $\mathbf{F}_I$ in the Morison equation, i.e., 2nd term in Equation (11). $\mathbf{F}_I$ is with the inertia coefficient $C_M\,(=1+C_A)$, and 1 and C_A are associated with contributions from the Froude-Krylov force and scattered wave force. The validity of the Morison equation is then assessed by comparing $\mathbf{F}_W$ and $\mathbf{F}_I$. Figures 3–4 show the comparison of horizontal/vertical $\mathbf{F}_W$ and $\mathbf{F}_I$ (wave force per unit length). Wave direction was fixed at 90°

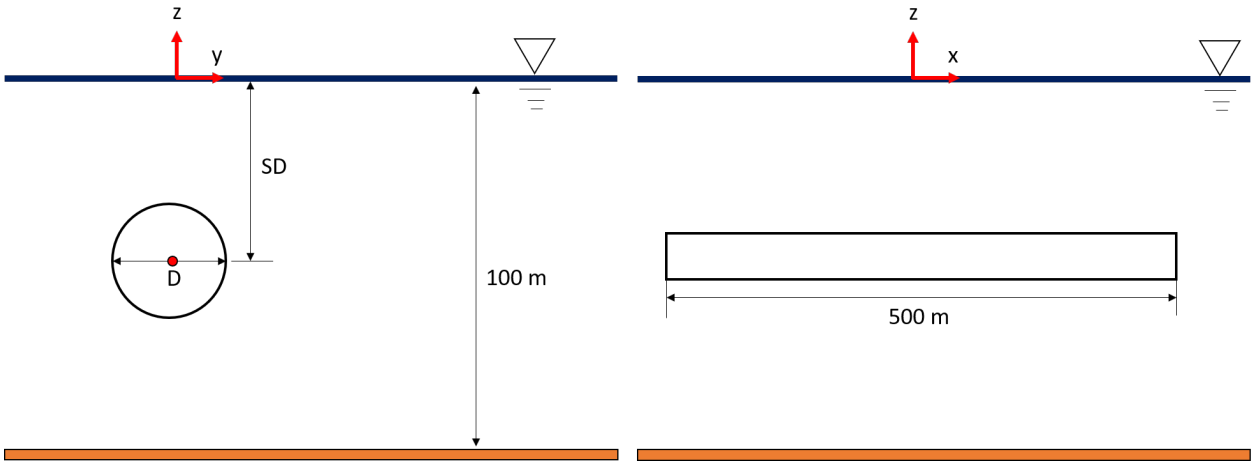

Figure 2. Configuration of a cylinder with fixed-fixed boundary condition (D denotes diameter; SD stands for submergence depth).

with respect to the positive x-axis, and $\mathbf{F_I}$ was calculated from the fixed body. At a low submergence depth of 20 m, which is close to free surface, trends and magnitudes of $\mathbf{F_W}$ are somewhat different from those of $\mathbf{F_I}$, as shown in Figure 3(a) and (c). The Morison model tends to overestimate the wave force at high frequencies of 0.7 rad/s or more. However, $\mathbf{F_W}$ and $\mathbf{F_I}$ are very close at higher submergence depths, regardless of the wave frequency range, as shown in Figure 3(b) and (d), which means that the Morson method can estimate the wave force accurately for deeply submerged cylinders even if the cylinder diameter is large. Moreover, the higher the submergence depth, the lower the importance of high-frequency wave forces since the wave kinematics decreases with submergence depth as a function of $\cosh k(z+H)$ for intermediate water and e^{kz} for deep water. As shown in Figure 4, the difference between the two forces is significantly reduced at a small diameter of 10 m even if the submergence depth is 20 m.

The previous results show that the Morison equation accurately estimates the wave inertia force at the large submergence depth and small cylinder diameter. It is well known that the Morison equation has a limitation, i.e., $D/L \le 0.2$. At the given water depth of 100 m and a cylinder diameter of 20 m, the wave frequency should be less than around 0.8 rad/s to be included in this condition. The scattered wave force $\mathbf{F_{SC}}$ is mainly associated with this limitation since the scattered wave force has a tendency to be important as the wave frequency increases. Figure 5 shows the comparison of the Froude-Krylov force $\mathbf{F_{FK}}$ and $\mathbf{F_{SC}}$ in the DMB method with half of $\mathbf{F_I}$ in the Morison method $(0.5\mathbf{F}_I = \mathbf{F_{MF}})$ that corresponds to $\mathbf{F_{FK}}$ in the DMB method. Wave kinematics for the Morison equation is estimated at the geometric center, while that for $\mathbf{F_{FK}}$ is based on the cylinder surface. At the given cylinder diameters, regardless of submergence depths, $\mathbf{F_{MF}}$ is similar to $\mathbf{F_{FK}}$, which means that kinematics estimation at the geometric center in the Morison method is still valid for this horizontal cylinder at the given frequency range. Then, as noticed in Figure 5(a), $\mathbf{F_{SC}}$ induces the difference between $\mathbf{F_W}$ and $\mathbf{F_I}$ only when submergence depth is low. In this case, the existence of free surface influences the calculation of $\mathbf{F_{SC}}$. No free-surface effect is detected when the submergence depth is 60 m due to a large distance between free surface and the cylinder.

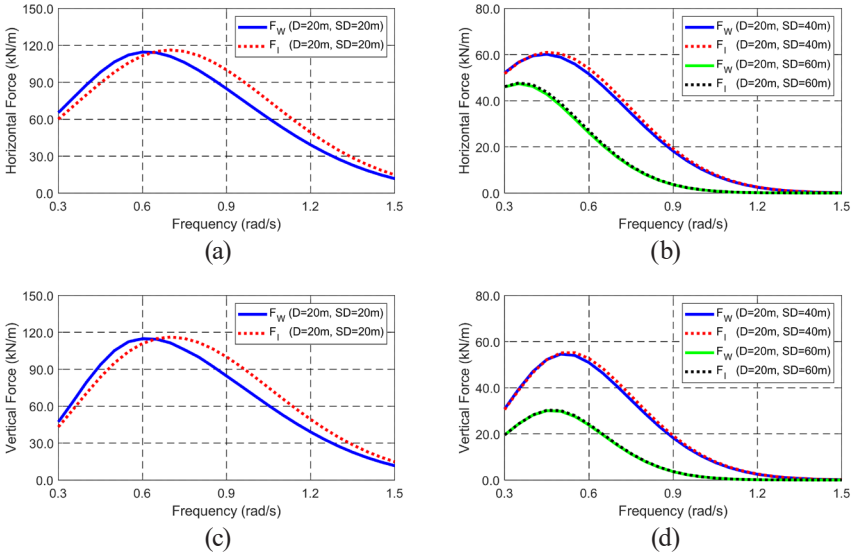

Figure 3. Comparison of horizontal/vertical $\mathbf{F_W}$ and $\mathbf{F_I}$ at a diameter of 20 m and different submergence depths.

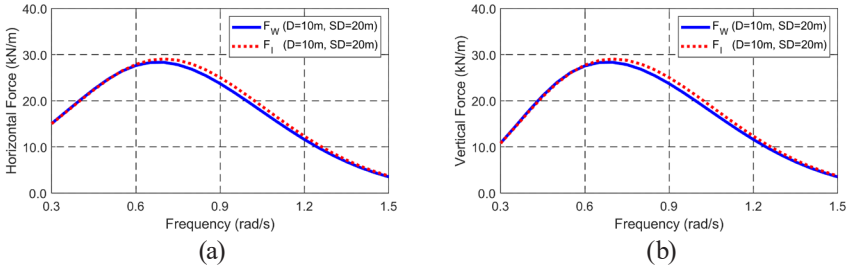

Figure 4. Comparison of horizontal/vertical $\mathbf{F_W}$ and $\mathbf{F_I}$ at a diameter of 10 m and a submergence depth of 20 m.

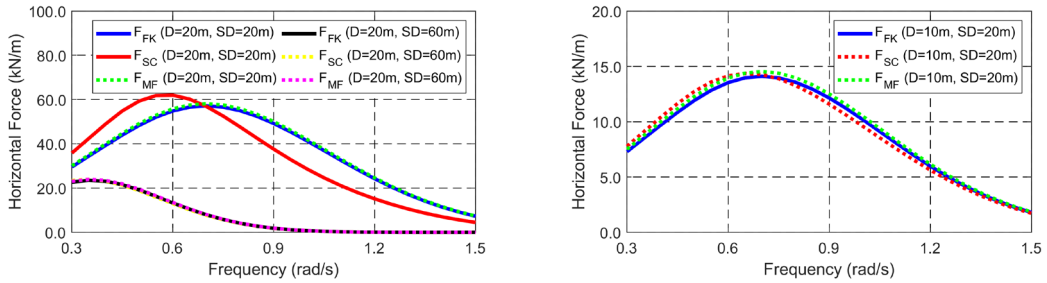

(a) (b)

Figure 5. Comparison of $\mathbf{F_{FK}}$, $\mathbf{F_{SC}}$, and $\mathbf{F_{MF}}$ at different diameters and submergence depths.

4.2 Modal Analysis

Next, modal analysis was conducted, and dry/wet mode shapes/natural frequencies were obtained. Wet mode shapes and natural frequencies require the added mass and hydrostatic restoring coefficient matrices. In the Morison equation, C_A is typically selected as 1 based on previous practices for the slender body [27]. However, the added mass is frequency-dependent, and wet mode shapes and natural frequencies can be changed. Tables 1-2 give dry and wet natural frequencies at different diameters and submergence depths. Morison and DMB models calculate similar dry natural frequencies with a maximum difference of 0.3%. Note that elements number for DMB and Morison methods for this example are 22 and 50, respectively. Since the Morison method is based on the lumped mass method, more elements are generally required than the high-order beam-based DMB method. Twenty-two finite elements in the DMB method are sufficient to represent the elastic behavior. For the wet mode, while both approaches are well matched at a small diameter of 10 m or a large submergence depth of 60 m, the large difference is observed when diameter and submergence depth are both 20 m. In this case, free surface plays some roles in the modification of wet natural frequencies by changing added mass. The maximum difference is increased to be 5.0%. In this regard, when a cylinder is large and close to free surface, special care should be made to evaluate wet natural frequencies.

Figure 6 shows the representative wet mode shapes of two methods at the diameter and submergence depth of 20 m. Even if there is a maximum difference of 5% in wet natural frequencies, there is no noticeable difference in the wet mode shape up to 3rd mode.

Table 1. Dry natural frequencies at different diameters.

D(m)	Direction	Mode#	Morison (rad/s)	DMB (rad/s)	Difference (%)
20	Horizontal	1	2.01	2.01	0.0
		2	5.51	5.51	-0.1
		3	10.73	10.73	-0.3
	Vertical	1	2.01	2.01	0.0
		2	5.51	5.51	-0.1
		3	10.73	10.73	-0.3
10	Horizontal	1	1.01	1.01	-0.3
		2	2.77	2.76	-0.2
		3	5.40	5.38	-0.3
	Vertical	1	1.01	1.01	-0.3
		2	2.77	2.76	-0.2
		3	5.40	5.38	-0.3

Table 2. Wet natural frequencies at different diameters and submergence depths.

D(m)	SD(m)	Direction	Mode#	Morison (rad/s)	DMB (rad/s)	Difference (%)
20	20	Horizontal	1	1.42	1.50	5.0
			2	3.91	4.04	3.4
			3	7.62	7.88	3.4
		Vertical	1	1.42	1.49	4.9
			2	3.91	4.06	3.7
			3	7.62	7.94	4.1
20	60	Horizontal	1	1.42	1.42	0.1
			2	3.91	3.93	0.5
			3	7.62	7.70	1.1
		Vertical	1	1.42	1.42	-0.3
			2	3.91	3.91	0.2
			3	7.62	7.68	0.8
10	20	Horizontal	1	0.71	0.72	0.3
			2	1.96	1.98	1.0
			3	3.82	3.86	1.0
		Vertical	1	0.71	0.72	0.3
			2	1.96	1.98	0.9
			3	3.82	3.85	0.7

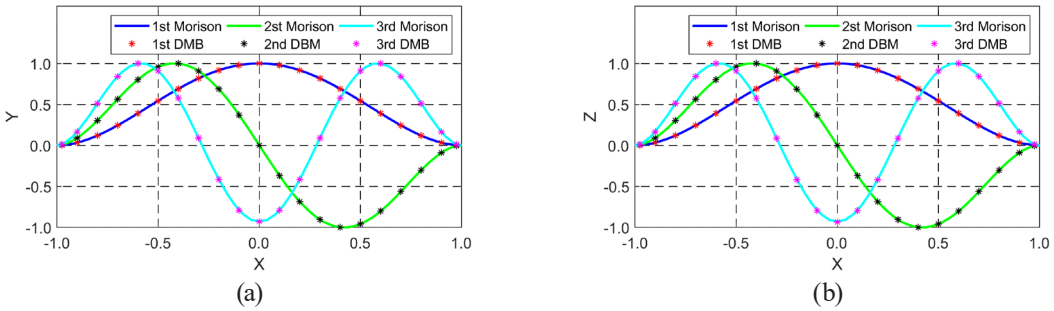

Figure 6. Wet mode shapes at the diameter and submergence depth of 20 m.

4.3 Global Behavior

In previous sections, there were two distinct differences between the DMB and Morison methods; at the diameter and submergence depth of 20 m, the existence of free surface changes the scattered wave force and added mass, which results in differences in total wave force and wet natural frequencies. In this section, global behaviors are further checked at different wave directions. The structural damping matrix based on Rayleigh damping $\mathbf{B_R}$ was added to deal with unrealistic resonant motions at natural frequencies. This study assumes a representative damping ratio of 5% for concrete structures at the fundamental horizontal and vertical natural frequencies.

Figure 7 shows the amplitude envelopes of horizontal and vertical displacements at the diameter and submergence depth of 0.2 m and wave direction of 90°. It turns out that the lowest mode shape is dominant for the given frequency range. In other words, the lowest horizontal and vertical natural frequencies for the DMB method are around 1.50 rad/s and 1.49 rad/s, and thus the lowest natural frequency is dominant for the given frequency range of 0.3 rad/s–1.3 rad/s. Since the Morison method overestimates the wave force at the high-frequency region, highly overestimated motions are seen, especially when wave frequency is close to the fundamental natural frequency.

Since the center has the most considerable movement related to the fixed-fixed boundary condition at both ends, results at the mid-length are presented in the later section.

Figure 8 shows the horizontal and vertical motions at the diameter of 20 m, different submergence depths of 20 m and 60 m, and wave direction of 90°. Again, the motion trend coincides with wave force. Overevaluated motions by the Morison method at the submergence depth of 20 m are observed, particularly in the high-frequency region. Since fundamental wet natural frequency for the Morison method is lower than that for the DMB method, resonant induced motion associated with high wave force is detected for the Morison method. On the other hand, the Morison method accurately estimates displacements for deeply submerged cylinders for the given frequency range since wet natural frequencies and wave forces between the two approaches coincide.

Finally, Figure 9 shows the horizontal and vertical motions at the diameter and submergence depth of 20 m and different wave directions of 30° and 60°. As wave direction is not perpendicular to the cylinder, there is an arrival time lag of input waves along the length, which can induce a phase cancellation effect where wave force in the different locations can be canceled out. The phase cancellation effect can be dominant in the high-frequency region. In this example, the lower the wave direction, the smaller the high-frequency motions. As shown in Figure 3, the DMB model estimates the higher wave excitation force for the range of 0.3 rad/s–0.7 rad/s; thus, the DMB model tends to produce higher motion than the Morison method for the given wave directions. Also, the magnitude of motions at the mid-length tends to decrease as the wave direction decreases.

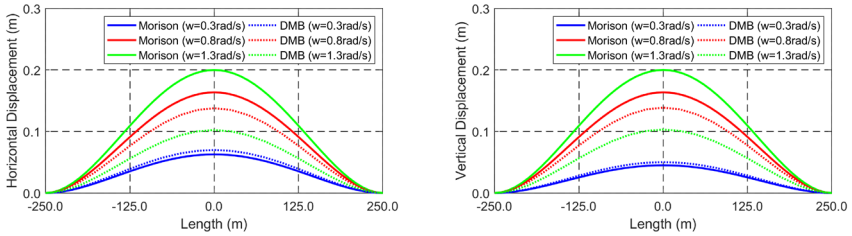

Figure 7. Amplitude envelopes of horizontal (a) and vertical (b) displacements (diameter of 0.2 m; submergence depth of 0.2 m; wave direction of 90°).

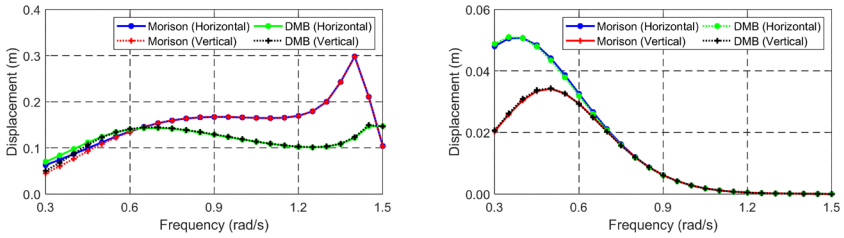

Figure 8. Amplitude of displacements at the mid-length and submergence depths of 20 m (a) and 60 m (b) (diameter of 0.2 m; wave direction of 90°).

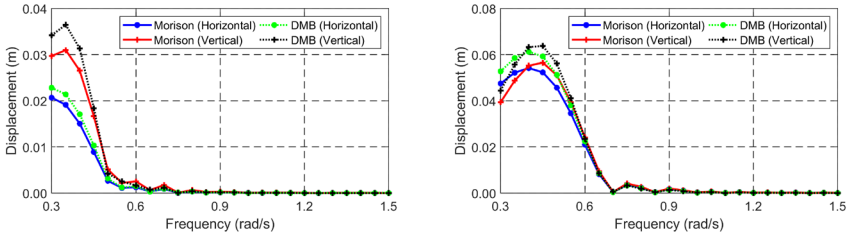

Figure 9. Amplitude of displacements at the mid-length and wave directions of 30° (a) and 60 ° (b) (diameter of 0.2 m; submergence depth of 0.2 m).

5. Conclusions

This study focuses on the hydro-elastic behaviors of a fully submerged horizontal cylinder in regular waves. The frequency-domain discrete-module-beam (DMB) method was developed; a continuous elastic floating structure is discretized into a certain number of rigid bodies while structural flexibility is modeled by beam elements with Euler-Bernoulli beam and Saint-Venant torsion; the hydrodynamic coefficients and wave forces were obtained from 3D potential theory. The time-domain Morison method was also employed; the Morison equation estimates wave forces and elastic behaviors are represented by massless axial, bending, and torsional springs. Various parametric studies on the cylinder diameter, submergence depth, and wave direction were conducted, and wave forces, dry/wet mode shapes/natural frequencies, and dynamic motions were analyzed. The results derived from this study are as follows:

(1) The presence of free surface tends to change the scattered wave force in the DMB model; the larger the diameter and the smaller the submergence depth, the greater the change in the scattered wave force. The overestimation of wave force in the high-frequency region is observed in the Morison model.

(2) Consideration of frequency-dependent added mass in the DMB method slightly changes the wet natural frequencies, whereas wet mode shapes of the two approaches are almost the same.

(3) The difference of wave forces and wet natural frequencies results in significant changes in the overall magnitudes of the dynamic motions. In this example, the Morison model tends to significantly overestimate dynamic motions around the fundamental wet natural frequency.

(4) Dynamics motions decrease with decreased wave direction, and high-frequency motion is reduced mainly due to the arrival time lag of incoming waves along the length, which induces phase cancellation of wave force.

Conflict of Interest

Author declares that there is no conflict of interest.

References

[1] Anastasopoulos, I., Gerolymos, N., Drosos, V., et al., 2007. Nonlinear response of deep immersed tunnel to strong seismic shaking. Journal of Geotechnical and Geoenvironmental Engineering. 133(9), 1067-1090.

[2] Chandrasekaran, S., Nannaware, M., 2014. Response analyses of offshore triceratops to seismic activities. Ships and Offshore Structures. 9(6), 633-642.

[3] Zhao, E., Dong, Y., Tang, Y., et al., 2021. Numerical investigation of hydrodynamic characteristics and local scour mechanism around submarine pipelines under joint effect of solitary waves and currents. Ocean Engineering. 222, 108553.

[4] Wang, Z., Yang, H., 2016. Parametric instability of a submerged floating pipeline between two floating structures under combined vortex excitations. Applied Ocean Research. 59, 265-273.

[5] Jin, C., Kim, M.H., 2018. Time-domain hydro-elastic analysis of a SFT (submerged floating tunnel) with mooring lines under extreme wave and seismic excitations. Applied Sciences. 8(12), 2386.

[6] Zou, P., Bricker, J.D., Chen, L., et al., 2022. Response of a submerged floating tunnel subject to flow-induced vibration. Engineering Structures. 253, 113809.

[7] Deng, S., Ren, H., Xu, Y., et al., 2020. Experimental study on the drag forces on a twin-tube submerged floating tunnel segment model in current. Applied Ocean Research. 104, 102326.

[8] Won, D., Seo, J., Park, J.S., et al., 2020. Internal force evaluation of a submerged floating pipeline under irregular waves. Journal of Marine Science and Technology. 28(6), 13.

[9] Nagavinothini, R., Chandrasekaran, S., 2020. Dynamic response of offshore triceratops with elliptical buoyant legs. Innovative Infrastructure Solutions. 5(2), 1-14.

[10] Morison, J., Johnson, J., Schaaf, S., 1950. The force exerted by surface waves on piles. Journal of Petroleum Technology. 2(05), 149-154.

[11] Lin, H., Xiang, Y., Yang, Y., et al., 2018. Dynamic response analysis for submerged floating tunnel due to fluid-vehicle-tunnel interaction. Ocean Engineering. 166, 290-301.

[12] Jin, C., Bakti, F.P., Kim, M., 2021. Time-domain coupled dynamic simulation for SFT-mooring-train interaction in waves and earthquakes. Marine Structures. 75, 102883.

[13] Muhammad, N., Ullah, Z., Choi, D.H., 2017. Performance evaluation of submerged floating tunnel subjected to hydrodynamic and seismic excitations. Applied Sciences. 7(11), 1122.

[14] Jin, C., Kim, S.J., Kim, M., 2021. Coupled time-domain hydro-elastic simulation for submerged floating tunnel under wave excitations. International Conference on Offshore Mechanics and Arctic Engineering. V006T006A023.

[15] Chakrabarti, S.K., Tam, W.A., 1975. Interaction of waves with large vertical cylinder. Journal of Ship Research. 19(01), 23-33.

[16] Chung, J.S., 2018. Morison equation in practice and hydrodynamic validity. International Journal of Offshore and Polar Engineering. 28(01), 11-18.

[17] Chang, S., Huang, W., Sun, H., et al., 2019. Numerical investigation of secondary load cycle and ringing response of a vertical cylinder. Applied Ocean Research. 91, 101872.

[18] Chandrasekaran, S., Jain, A., Gupta, A., 2007. Influence of wave approach angle on TLP's response. Ocean Engineering. 34(8-9), 1322-1327.

[19] Li, Y.S., Zhan, S., Lau, S., 1997. In-line response of a horizontal cylinder in regular and random waves. Journal of fluids and structures. 11(1), 73-87.

[20] Chen, B., Lu, L., Greated, C.A., et al., 2015. Investigation of wave forces on partially submerged horizontal cylinders by numerical simulation. Ocean Engineering. 107, 23-31.

[21] Jin, C., Kim, M., 2021. The effect of key design parameters on the global performance of submerged floating tunnel under target wave and earthquake excitations. CMES-Computer Modeling in Engineering & Sciences. 128(1), 315-337.

[22] Bakti, F.P., Jin, C., Kim, M.H., 2021. Practical approach of linear hydro-elasticity effect on vessel with forward speed in the frequency domain. Journal of Fluids and Structures. 101, 103204.

[23] Lu, D., Fu, S., Zhang, X., et al., 2016. A method to estimate the hydroelastic behaviour of VLFS based on multi-rigid-body dynamics and beam bending. Ships and Offshore Structures. 14(4), 354-362.

[24] Wei, W., Fu, S., Moan, T., et al., 2017. A discrete-modules-based frequency domain hydroelasticity method for floating structures in inhomogeneous sea conditions. Journal of Fluids and Structures. 74, 321-339.

[25] Jin, C., Bakti, F.P., Kim, M., 2020. Multi-floater-mooring coupled time-domain hydro-elastic analysis in regular and irregular waves. Applied Ocean Research. 101, 102276.

[26] Orcina, 2020. OrcaFlex User Manual Version 11.0 d.

[27] Faltinsen, O., 1993 Sea loads on ships and offshore structures. London, UK: Cambridge university press.